Cell Reports
Physical Science

CellPress

Article

Metastability and Reversibility of Anionic Redox-Based Cathode for High-Energy Rechargeable Batteries

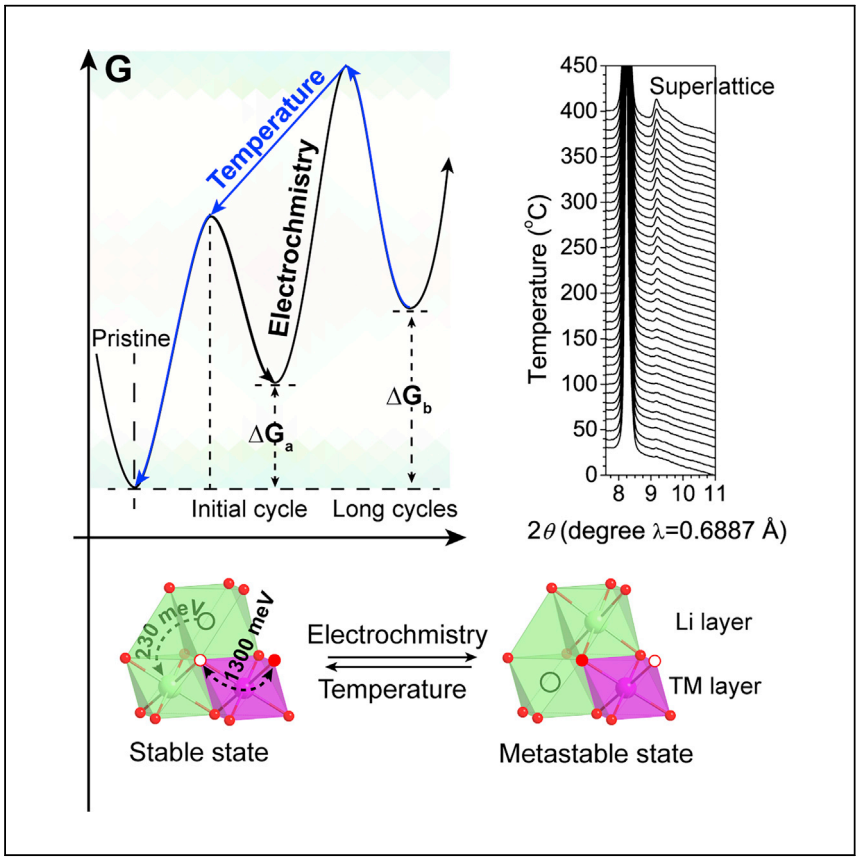

Efforts to develop next-generation cathodes with improved energy density and cycling life are essential for the widespread adoption of electric vehicles. Qiu et al. demonstrate the unique metastable structure of a cycled anionic redox-based cathode and the impact of thermal energy on energy recovery after extended cycles.

Bao Qiu, Minghao Zhang, Seung-Yong Lee, ..., Dong Zhou, Zhaoping Liu, Ying Shirley Meng

liuzp@nimte.ac.cn (Z.L.)
shmeng@ucsd.edu (Y.S.M.)

HIGHLIGHTS

The structure of the cycled Li-rich layered oxide is unique metastable

Diverse structural defects are responsible for the voltage decay

Structure and voltage are reversible through mild heat treatment

Qiu et al., Cell Reports Physical Science *1*, 100028
March 25, 2020
https://doi.org/10.1016/j.xcrp.2020.100028

Cell Reports
Physical Science

CellPress

Article

Metastability and Reversibility of Anionic Redox-Based Cathode for High-Energy Rechargeable Batteries

Bao Qiu,[1,7] Minghao Zhang,[2,7] Seung-Yong Lee,[3] Haodong Liu,[2] Thomas A. Wynn,[2] Lijun Wu,[3] Yimei Zhu,[3] Wen Wen,[4] Craig M. Brown,[5] Dong Zhou,[6] Zhaoping Liu,[1,*] and Ying Shirley Meng[2,8,*]

SUMMARY

Great focus has recently been placed on anionic redox, to which high capacities of Li-rich layered oxides are attributed. With almost doubled capacity compared with state-of-the-art cathode materials, Li-rich layered oxides still fall short in other performance metrics. Among these, voltage decay upon cycling remains the most hindering obstacle, in which defect electrochemistry plays a critical role. Here, we reveal that the metastable state of cycled Li-rich layered oxide, which stems from structural defects in different dimensions, is responsible for the voltage decay. More importantly, through mild thermal energy, the metastable state can be driven to a stable state, bringing about structural and voltage recovery. However, for the classic layered oxide without reversible anionic redox, thermal energy can only introduce cation disordering, leading to performance deterioration. These insights elucidate that understanding the structure metastability and reversibility is essential for implementing design strategies to improve cycling stability for high-capacity layered oxides.

INTRODUCTION

In recent decades, rechargeable lithium-ion batteries (LIBs) have commercially dominated the portable electronics market.[1] Moreover, LIBs are turning into the most encouraging market areas for powering electric vehicles. However, the energy density and cycle life of state-of-the-art LIBs have to be further enhanced to satisfy expectations for transportation applications.[2] The current commercial market for cathode materials is dominated by classic layered lithium transition metal (TM) oxides, e.g., $LiCoO_2$, $LiNi_{1/3}Mn_{1/3}Co_{1/3}O_2$, and $LiNi_{0.8}Co_{0.15}Al_{0.05}O_2$. Their relatively low capacities have been one of the major bottlenecks to achieve high-energy density in LIBs.[3] These primary commercial materials solely rely on cationic redox activity, which places a fundamental limit on the available capacity. Given these considerations, the recent discovery of reversible anionic redox has created a paradigm for design of novel cathode chemistries. For example, substitution of the TM by Li enables Li-rich Mn-based layered oxides with composition $xLi_2MnO_3 \cdot (1\text{-}x)LiTMO_2$ to exhibit reversible capacities exceeding 300 mAh g^{-1} versus a practical capacity of ~150 mAh g^{-1} for the commercial $LiCoO_2$[4–8] (Figures 1A and 1B). In order to further utilize oxygen activity, Li/O ratio needs to be increased in the designed material,[8] where the majority of the oxygen bonding environment is Li-O-Li configuration and reversible capacity is dominated by the oxygen redox.[9] Li_3NbO_4-based disordered rock salt is thus selected in Figure 1B to compare the performance with Li-rich layered oxide materials. As shown in Figure 1C, Li-rich layered oxide is the most promising cathode to satisfy demands of future electric vehicle energy-storage

[1]Ningbo Institute of Materials Technology and Engineering, Chinese Academy of Sciences, Ningbo 315201, P.R. China

[2]Department of NanoEngineering, University of California, San Diego, La Jolla, CA 92093, USA

[3]Department of Condensed Matter Physics and Materials Science, Brookhaven National Laboratory, Upton, NY 11973, USA

[4]Shanghai Synchrotron Radiation Facility, Shanghai Institute of Applied Physics, Chinese Academy of Sciences, Zhangjiang High-Tech Park, Pudong New Area, Shanghai 201204, P.R. China

[5]National Institute of Standards and Technology, Center for Neutron Research, 100 Bureau Drive, Gaithersburg, MD 20899-6102, USA

[6]University of Muenster MEET Battery Research Center, Corrensstrasse 46, 48149 Muenster, Germany

[7]These authors contributed equally

[8]Lead Contact

*Correspondence: liuzp@nimte.ac.cn (Z.L.), shmeng@ucsd.edu (Y.S.M.)

https://doi.org/10.1016/j.xcrp.2020.100028

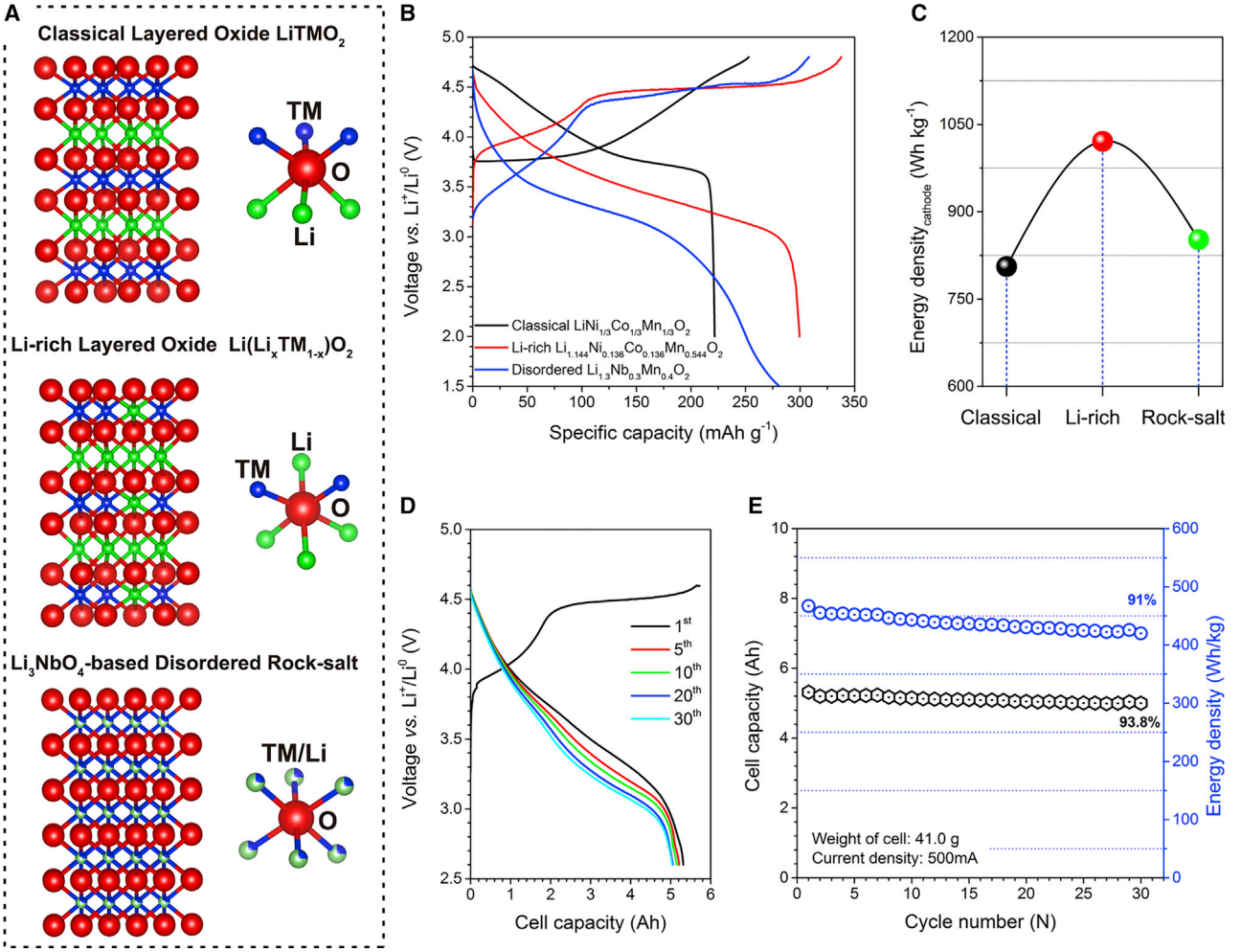

Figure 1. Structure and Electrochemical Performance Comparison of Cathode Materials for Next-Generation High-Energy Rechargeable Batteries

(A) Schematic illustration of the crystal structure of classic layered oxide $LiTMO_2$, Li-rich layered oxide $Li(Li_xTM_{1-x})O_2$, and Li_3NbO_4-based disordered rock salt (green, Li; blue, TM; red, oxygen).

(B) Representative charge and discharge voltage profiles at 0.1 C-rate of different cathode materials with metallic Li as the counter electrode, where the voltage ranges were set to be 2.0–4.8 V versus Li^+/Li^0 for $LiNi_{1/3}Co_{1/3}Mn_{1/3}O_2$ and $Li_{1.144}Ni_{0.136}Co_{0.136}Mn_{0.544}O_2$, and 1.5–4.8 V versus Li^+/Li^0 for $Li_{1.3}Nb_{0.3}Mn_{0.4}O_2$.

(C) Discharge energy density comparison at cathode level of different layered oxides tested with metallic Li as the counter electrode.

(D and E) Voltage profiles (D), specific energy (E), and cycling retention at the cell level (E) of Li-rich layered oxide cathode with Li metal as the anode, where the voltage range was set to be 2.6–4.6 V versus Li^+/Li^0.

market for higher specific energy. It is noteworthy that we have recently demonstrated over 450 Wh kg^{-1} specific energy at the cell level when Li metal anode is applied for Li-rich layered oxide cathode (Figures 1D and 1E).

Advanced materials are frequently double-edged swords—such materials showing exceptional utility are typically accompanied by remarkable issues. The major limitations of anionic redox are the serious structural degradation and energy attenuation during battery cycling (Figures 1D and 1E). In order to activate oxygen redox, batteries with lithium-rich layered oxide cathode have to be charged over 4.5 V versus Li^+/Li^0. This activation unfortunately results in structural transformation in the form of defects formation.[10–15] This structural transformation is not fully reversible during each electrochemical cycle, leading to voltage hysteresis and

energy inefficiency.[15] At the same time, a continuous voltage decay occurs, resulting from structural degradation, which complicates the battery management systems and plagues their implementation in practical batteries.[16]

Structure degradation induced by the defects formation and its influence on the electrochemical performance have been investigated from a variety of interrelated viewpoints: oxygen vacancies were found to form near the material surfaces by scanning transmission electron microscopy (STEM) and electron energy loss spectroscopy (EELS);[17] these oxygen vacancies facilitate migration of TM with broken TM-O bonds from the under-coordinated octahedral site of TM layers to the fully coordinated tetrahedral/octahedral sites in the Li layer;[18,19] lithium local environment changes due to formation of lithium "dumbbells" were predicted by computation to involve Li occupation of tetrahedral sites in the lithium layers;[20] the above migrations finally lead to the defect-spinel phase generation on the particle surfaces and sub-surfaces; dislocation network or stacking sequence changes were also observed in nanoparticles of lithium-rich layered oxide material by Bragg coherent X-ray diffractive imaging (BCDI).[12] Although all these inhomogeneities have been ascribed to voltage decay,[21] further investigations are needed to demonstrate defect formation is the direct causation for voltage decay.

Based on the range of degradation mechanisms exhibited, strategies including surface modification[6,22,23] and elemental substitution,[24,25] among others, have been proposed to mitigate defect formation and maintain structural order. Despite these incremental improvements, the voltage fading is still inevitable and remains a challenge that will require further effort to overcome.[26] All the previous studies implicate, upon electrochemical activation, Li-rich layered oxides would exhibit some extent of voltage fade no matter what testing conditions or modification strategies are presented. After intense efforts, it is time to carefully consider whether the voltage decay is an intrinsic and unalterable consequence of anionic activity so that this anionic redox will ever empower the future of LIBs. More specifically, three questions need to be answered: (1) Is the degraded structure after cycling caused by defects generation energetically stable or metastable? (2) If it is metastable, under what circumstance can defects be at least partially eliminated so that the cycled structure is recovered to a stable state? (3) If the structure can be recovered, will the original redox potential be restored?

Toward answering these questions, we illustrate a direct causation between defect generation and voltage decay in lithium-rich layered oxides. More importantly, we demonstrate the cycled state with defects is a dynamical system other than the state of least energy. This unique metastable cycled state resulting from defects is not only the origin of voltage decay but also provides a clue to design pathway to address the voltage decay issue. An effective approach, mild heat treatment, is thus found to drive the metastable state close to the pristine state. This treatment effectively recovers the local Li-excess environment around oxygen, oxygen stacking sequence, and eliminates microstrain associated with various defects. As a result, the charging voltage profile once more shows a plateau region, and the average discharge voltage is restored from the cycled cathode. In contrast, for the cycled cathode material without anionic redox, thermal energy can only introduce cation disordering, which follows the basic entropy principle. Both theoretical predictions and experimental characterizations illustrate that the structure metastability and defect removal are decisive in the structure and voltage recovery.

RESULTS

Demonstration of Cycled Structure Metastability

The synthesis process of lithium-rich layered oxide $Li[Li_{0.144}Ni_{0.136}Co_{0.136}Mn_{0.544}]O_2$ (denoted as LR-NCM) is described in Synthesis of Difference Cathode Materials. Morphology and phase purity were confirmed by scanning electron microscopy (SEM, Figure S1) and synchrotron X-ray diffraction (SXRD, Figure S2) and are consistent with previous work. By fabricating the 18650-type full battery as detailed in the Experimental Procedures, a large amount of the cycled cathode material was obtained for further characterization and treatment. Lithium titanate $Li_4Ti_5O_{12}$ (LTO) was selected as the anode in the 18650-type battery since it exhibited better cycling performance in this configuration, compared with lithium metal anode. The typical capacity-voltage profiles of LR-NCM oxide at 0.1 C-rate are presented in Figure 2A. Voltage profiles correlate with transformation of the materials structure as a function of lithiation state. It shows the feasibility to remove nearly 88.4% of Li (corresponding to a capacity of 313 mAh g^{-1}) from the cathode structure and also the characteristic sloped and plateaued region during the first charge. However, only 84.5% of extracted Li (corresponding to a capacity of 265 mAh g^{-1}) could be reinserted by an S-type discharge curve. Compared with the first charge, the smaller capacity and lower voltage in the first discharge suggest that the structure is not fully reversible after the first cycle. Indeed, the intensity of superlattice peaks in SXRD patterns, which represent the degree of long-range structural order, reduces significantly after the initial cycle (Figure S3). Figure 2B shows the normalized discharge voltage profiles of the LR-NCM/LTO full cell for 50 cycles. The discharge voltage exhibits a continuous decrease with cycling, which suggests structure degradation continues with extended cycles. Not surprisingly, superlattice peaks almost vanish after 50 cycles (Figure S3).

It is well understood that the structure degradation in LR-NCM during electrochemical cycling refers to different types of defect formation while essentially preserving the original layered phase.[12,21,27,28] In general, the presence of a high concentration of defects within a crystal structure can induce a thermodynamically unfavorable or metastable state.[29] To directly investigate whether the cycled material is in a metastable state, thermogravimetric (TG) and differential thermal analysis (DTA) were performed on the cycled sample (Figures 2C and 2F) in air, heated until 400°C to prevent phase transition from layer type to spinel or rocksalt type.[30] The samples after the initial cycle and after 50 cycles both show two reaction regions through the temperature range: (1) an endothermic process from 30°C to 150°C, which corresponds to the decomposition and/or volatilization of organic compounds and/or $LiPF_6$ salt formed and/or left on the electrode surface during the initial cycle,[31] and (2) an exothermic process from 150°C to 400°C, which can be ascribed to structural reorganization. Considerable heat release was detected in this exothermic process, which implies the material transitions to a lower energy state driven by a temperature higher than 200°C (the onset temperature of the exothermic peak). In other words, the cycled material before thermal interaction is in an energetically metastable state. The experiment was performed both in air and an inert nitrogen environment, showing no notable change, which suggests that atmospheric oxygen does not participate in the reaction (Figure S4A). Additionally, the weight loss through the whole temperature range is primarily attributed to the binder and byproducts decomposition in the cycled electrode (Figures S4B and S4C).[30]

In situ temperature-dependent SXRD (TD-SXRD) was then applied to reveal the structural evolution during the heat treatment of the cycled sample. Figure 2D shows

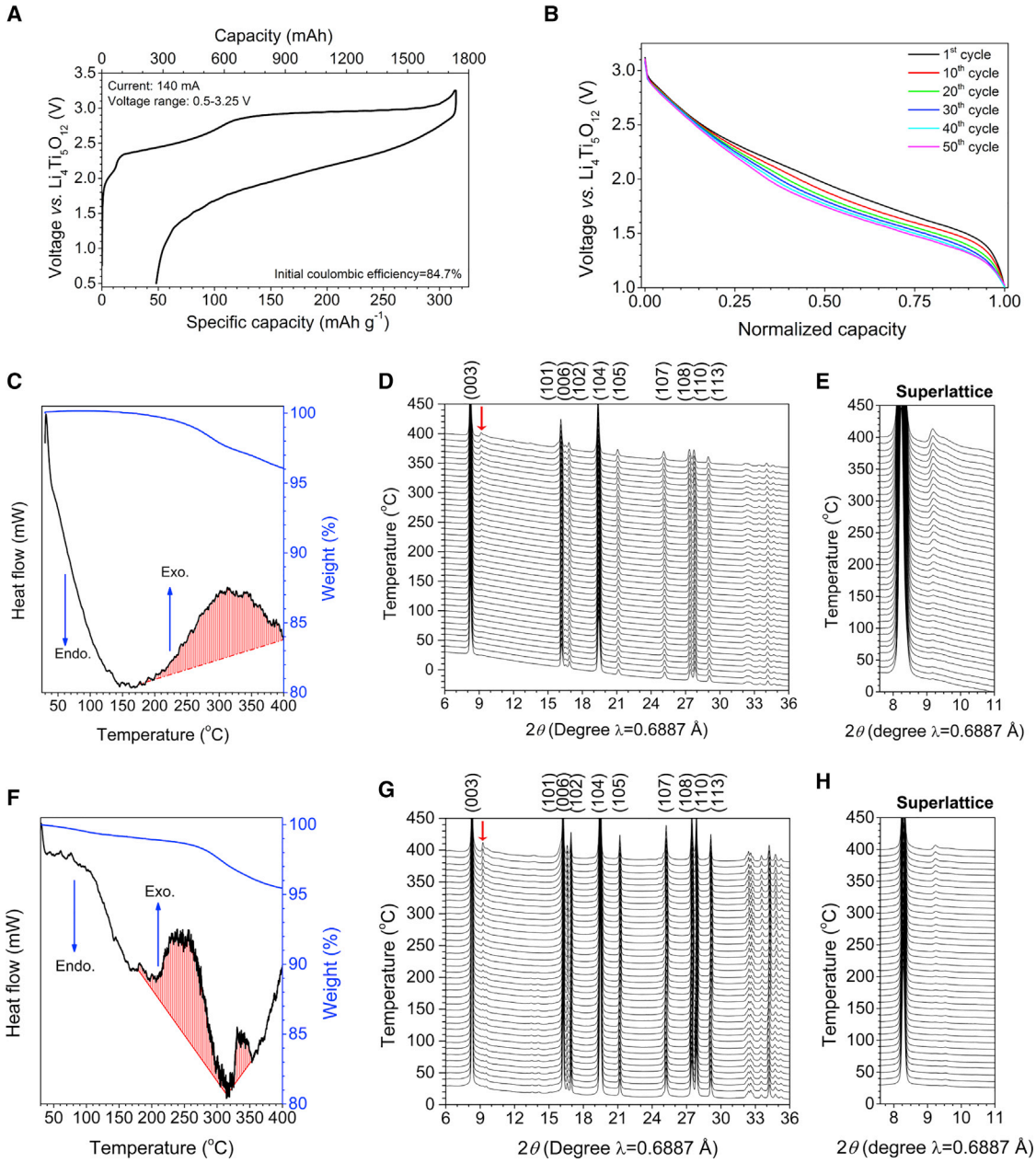

Figure 2. Characterization of Metastable Structure Formation after Cycling of Lithium-Rich Layered Oxide

(A) First charge-discharge voltage profiles of LR-NCM obtained from an 18650-typed full battery at 0.1 C-rate between 3.25 and 0.5 V versus LTO.

(B) Normalized discharge voltage profiles of LR-NCM, where the full battery was cycled within the voltage range of 1.0–3.25 V versus LTO at 0.1 C.

(C and F) TG and DTA analysis of the electrode after initial cycle (C) and after 50 cycles (F) in air.

(D and G) *In situ* TD-SXRD of the electrodes after initial cycle (D) and after 50 cycles (G).

(E and H) Enlarged TD-SXRD patterns related to the superlattice ordering of the electrodes after initial cycle (E) and after 50 cycles (H).

SXRD patterns of the sample after the first cycle during *in situ* annealing between 25°C and 400°C, clearly showing no phase transition. The most notable change is the intensity of the superlattice peaks. The superlattice peaks around $2\theta = 9.3°$ gradually reappear with increasing temperature (Figure 2E), indicating reordering of the bulk structure. To verify that the heat treatment would effectively reorder the structure after extended cycles, *in situ* SXRD was performed for samples after

50 cycles within the same temperature range (Figures 2G and 2H). The same trend is confirmed based on the reappearance of the superlattice peaks. The evolution of microstrain during the heat treatment was extracted by examining Bragg peak broadening observed in the SXRD patterns through the Williamson-Hall method.[32] The microstrain was observed to gradually increase when the cycled samples were heated from room temperature to 125°C due to the thermal expansion (Figures S5A and S5C). After the heating temperature exceeded 150°C, the microstrain suddenly decreased, reaching its minimum value at a temperature around 300°C. Interestingly, the temperature region accompanied by strain release correlates with the exothermic region in the DTA test. Such strain release once more suggests heat treatment is an effective method to drive the free energy of the cycled structure lower, to a more stable state.

Demonstration of Cycled Structure Reversibility

During cycling, a range of defects form in the LR-NCM, which resulted in increased disorder of the bulk structure. The reappearance of the superlattice peaks during heat treatment is a strong indication of defect elimination. To further investigate the influence of heat treatment on defect elimination, neutron diffraction (ND) was conducted on the pristine and cycled LR-NCM samples. The ND patterns with Rietveld refinement (refined with a solid solution of "R-3 m" symmetry) for each condition are shown in Figures 3A–3D. The lattice parameters of pristine LR-NCM are $a = b = 2.8517$ Å, and $c = 14.234$ Å. After cycling, the unit cell volume is shown to expand, with all lattice parameters increasing. However, after annealing at 300°C, both a and c lattice are observed to decrease ($a = b = 2.8527$ Å, and $c = 14.292$ Å). This trend deviates from the common trend of material thermal expansion, having shown structural relaxation with lattice contraction approaching that of the pristine state. This lattice contraction phenomenon during heat treatment is confirmed by TD-SXRD refinement (Figures S5B and S5D), also pinpointing the structural relaxation to occur between 125°C and 300°C—again consistent with the temperature range for strain release.

Since lithium has a negative scattering cross-section compared to oxygen and most other elements in neutron scattering, we can gauge quite well the lithium and oxygen content in the TM layer. Lithium occupancy in the TM layer and oxygen occupancy obtained from ND refinement are shown in Figures 3E and 3F. After the initial cycle, lithium migration from the TM layer is shown to be largely irreversible, with only 32% residual lithium occupation compared with the pristine state. Even fewer lithium ions can be found in the TM layer after 50 cycles. Additionally, oxygen vacancies are observed in the cycled sample, which results in a large fraction of under-coordinated TM ions. These unstable TM ions can potentially migrate to fully coordinated octahedral sites nearby.[17] Irreversible Li occupancy in the TM layer together with TM ion migration dramatically alters the cation ordering in the TM layer accounting for the observed the structural disorder in terms of the disappearance of the superlattice peak. Interestingly, heat treatment of the sample after one cycle increases the Li occupancy in the TM layer to 72% compared with the pristine state (Table S1). However, TM occupancy in the TM layer does not change obviously. So most of TM migration has to occur within the TM layer, if there is any. Figure S6 presents the Fourier-transform (FT) magnitudes of the extended X-ray absorption fine structure (EXAFS) spectra of their k3-weighted Mn K-edge annealing at different temperatures. This result confirms that the local environment of manganese in the samples annealing at different temperatures has undergone large changes with respect to that of manganese in the initially cycled sample. For example, when the temperature increases up to 200°C, the amplitudes

CellPress

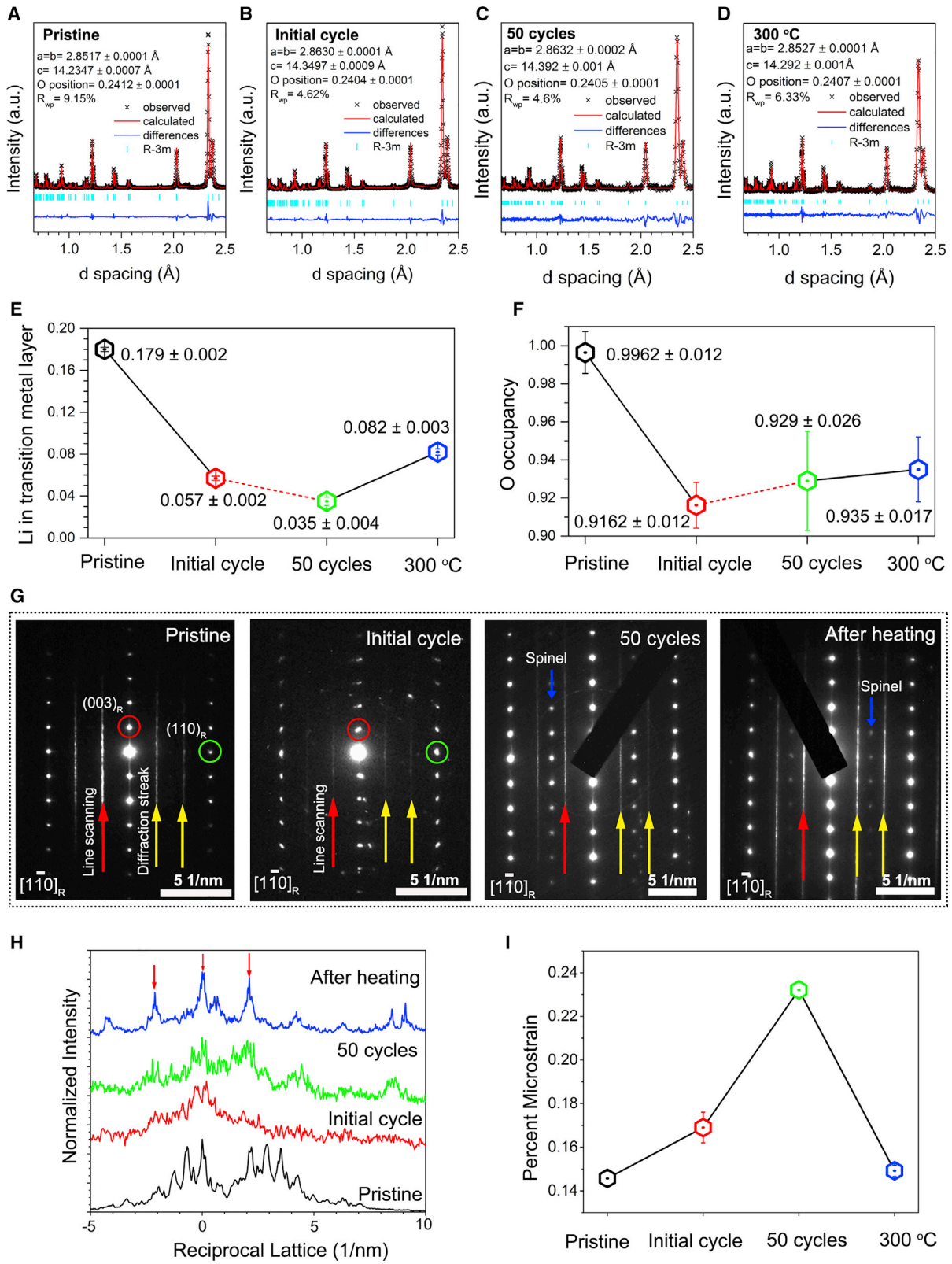

Figure 3. Cycled Structure Reversibility Demonstration after Heat Treatment of Lithium-Rich Layered Oxide

(A–D) Refined ND of pristine LR-NCM (A), LR-NCM after the initial cycle (B), after 50 cycles (C), and after 50 cycles annealed at 300°C for 1 h (D), respectively.

of both the first-shell and second-shell increases, even up to the same intensity as in the pristine state at 300°C. The higher Mn-O and Mn-TM intensity indicates the formation of more ordered structure in the TM layer during the heat treatment. Consequently, the specific Li-O-Li configurations, which are derived from the excess Li in the TM layer, recover after heat treatment, leading to the electrochemically active oxygen states in Li-rich layered oxide.[5] The elimination of lithium vacancies in the TM layer recovers local Li-excess environments around oxygen, which is considered to be crucial for oxygen redox potential.[5] Note that the concentration of oxygen vacancies has no obvious change within the error range during the heat treatment. However, this observation does not exclude the possibility of oxygen vacancies local migration, which is proposed to be a key for lithium reinsertion to the TM layer.

Another type of defect, stacking faults were observed through (S)TEM for pristine LR-NCM as shown in Figure S7. Fairly intense diffraction streaks arising from the stacking faults were recorded in electron diffraction (ED) patterns in Figure 2G.[33] After cycling, atomic displacements in and across TM layers are common enough that it shows a foggy atomic resolution imaging (Figure S7). Correspondingly, the diffraction streaks in the ED pattern are more diffuse, indicating reduced ordering along the layers stacking direction. After heat treatment at 300°C for 1 h, the bulk structure maintains the layered phase although the surface is transformed to a spinel-type structure (Figure S8). More importantly, the diffraction spots along the streaks in ED pattern become more obvious compared with the cycled bulk structure (Figure 3G). To show the ED changes clearly from different samples, the diffraction streak intensities were quantified from line profiles, and profile source positions are indicated by red arrows in Figure 3G. The measured peak sharpness increases after the heat treatment, as compared with the samples after cycling (Figure 3H). This observation is replicated by ED simulation of LR-NCM under a variety of stacking fault concentrations using SingleCrystal software (Figure S9). The ED analysis implies the stacking faults generated in the bulk structure during electrochemical cycling can be at least partially eliminated by the heat treatment, as structural ordering along the layers stacking direction is partially restored.

In general, thermal energy flows into the cycled material during heat treatment, which should result in entropy and disorder increase. However, the disorder of the cycled structure decreases after heat treatment as revealed by ND and TEM/ED results. Structure reordering during heat treatment has two main characteristics: (1) lithium ion reinsertion to the TM layer, and (2) reduced stacking fault concentration along the *c* axis. These defect elimination processes dramatically reduce the accumulated strain during cycling (Figure 3I). After heat treatment, the structure of the cycled material is driven close to the original pristine state in terms of unit cell volume (Figures S5E and S5F), Li occupancy in the TM layer, stacking fault concentration, and percentage of microstrain. These changes together account for the reemergence of superlattice peaks in SXRD patterns (Figures 2D and 2G), demonstrating the structure recovery of the cycled material.

(E) Changes of the Li ions occupancy in the TM layer for different samples obtained from ND refinement.
(F) Changes of the oxygen occupancy for different samples obtained from ND refinement.
(G) ED pattern for different samples. The elongation of these spots are along $[1\text{–}10]_R$ direction. The spots indicated with yellow arrows represent (110), (020), and (−110) lattice plane of the monoclinic Li_2MnO_3 (donated as M). The spot marked by a red circle is shared by $(003)_R$ lattice plane of the rhombohedral (donated as R) phase. The spot marked by a green circle is shared by $(110)_R$ lattice plane of the rhombohedral phase.
(H) Normalized intensity of reciprocal lattice from line-scanning position presented by red arrows in (G).
(I) Changes of percentage of microstrain for different samples, obtained from SXRD.
Error bars in (E), (F), and (I) represent standard errors.

Demonstration of Voltage Recovery

To assess the effect of structure recovery on electrochemical performance, coin cells were assembled using the heat-treated cathode materials and Li metal as anode. Figure S10 shows the charge-discharge curves for the initially cycled LR-NCM material after annealing at different temperature in the voltage range of 2.0–4.6 V versus Li^+/Li^0. The plateau region at approximately 4.5 V during charging gradually appears with an increasing annealing temperature. The charging plateau due to the excess Li in the TM layer is believed to originate from the linear Li-O-Li configuration.[5] The reappearance of charging plateau is thus consistent with Li ion reinsertion into the TM layer during the annealing process, as confirmed by ND results. As shown in Figure S11, the initially cycled LR-NCM followed by annealing at 300°C shows the largest Li concentration in the TM layer, which accounts for the longest plateau among the samples with different annealing temperature. No obvious reduction peak changes were found in the differential capacity versus voltage (*dQ/dV*) plots (Figure S10B), which once more demonstrates the original layered phase is preserved after annealing. Although the average discharge voltage shows a similar decay trend with subsequent cycles (Figure S10C), the starting discharge voltage increases from 3.575 to 3.667 V after annealing. In addition, annealing atmosphere and length of the annealing time were shown to have little impact on the electrochemical performance (Figure S12).

The above electrochemical results shed light on voltage recovery in LR-NCM after long-term cycling. Figure 4A shows the first charge-discharge curves of electrode after 50 cycles annealed at different temperature. The same trend as the electrode after one cycle is found with increased annealing temperature: not only does the charge plateau region reappear but also the reduction peak in the *dQ/dV* plots (inset in Figure 4A) clearly shifts toward higher voltage. The average discharge voltage shows a great increase from 3.370 to 3.628 V (Figure 4B). This corresponds to nearly 10% increase of energy density. When compared to the sample without heat treatment, although the average discharge voltage retention is similar for the subsequent cycles, the actual discharge voltage is much higher for each cycle. The heat-treated sample also shows better capacity retention in subsequent cycles. The charge-discharge curves for different cycles are provided in Figure S13. Note that the first electrochemical cycle after heat treatment is almost identical, whether the electrode is cycled once or 50 times previously (Figure 4C). In short, heat treatment successfully provides a path to recover the average voltage after long-term cycling for LR-NCM material. In addition, to address the concern of TM valence state changes during heat treatment, X-ray absorption spectroscopy (XAS) results for different samples are shown in Figure S14. No obvious edge shift or feature changes were found for TM, demonstrating that TM valence state remains almost the same during annealing process. In other words, the effect of voltage recovery originates from structure reordering instead of TM oxidation state changes.

DISCUSSION

At this point, we are still left with one important question: what is the dominant factor for the voltage decay in Li-rich layered oxides? There is an apparent controversy in the current understanding of the voltage fade. Hy et al.[34] observed the generation of Li_2CO_3 and Li_2O as a result of lattice O^{2-} loss for LR-NCM materials. These surface side reactions were ascribed to be the key to the cycle instability of the materials. Yan et al.[35] found a sequential surface structural change from layered to spinel with increasing cycles up to 100 cycles. Boulineau et al.[36] reported the thickness of the surface spinel phase remained at 2–3 nm even after 50 cycles.

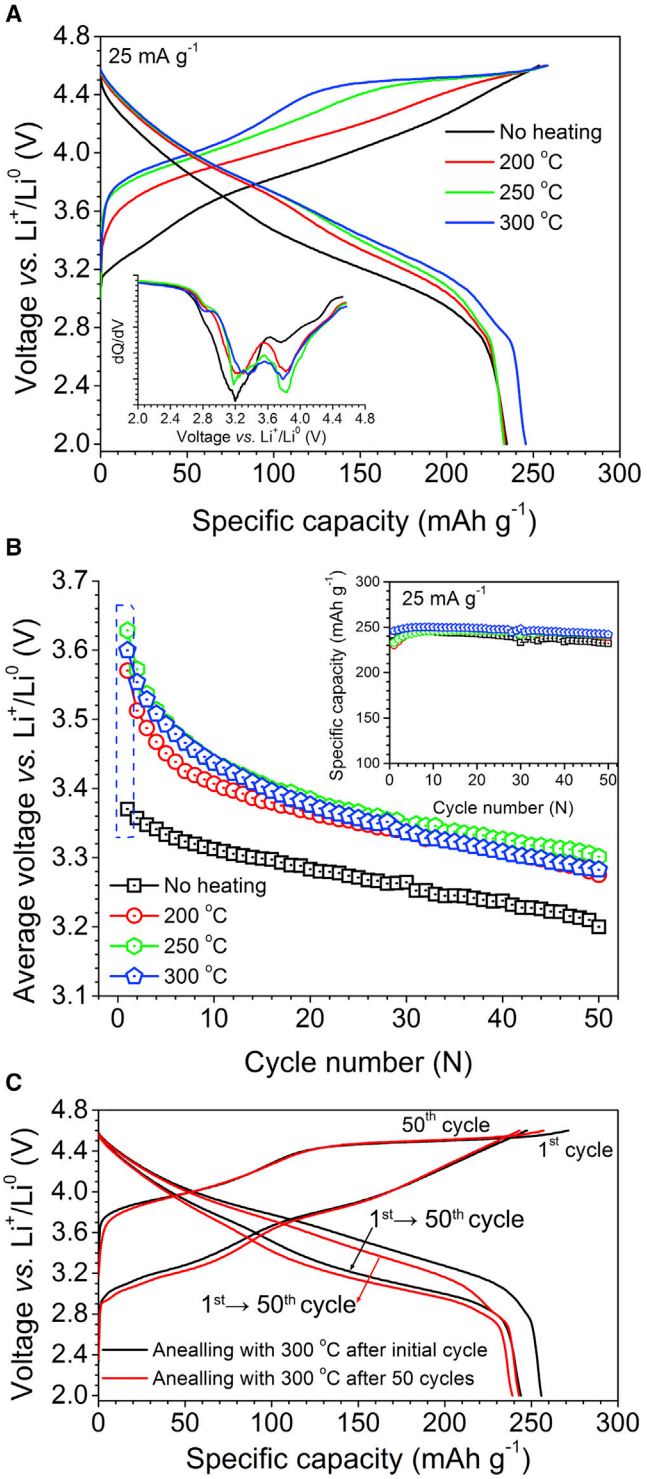

Figure 4. Voltage Recovery Demonstration after Heat Treatment of Cycled Lithium-Rich Layered Oxide

(A) The first charge-discharge curves of the electrode after 50 cycles annealed at different temperature. The inset shows dQ/dV plots of the discharge curves.

(B) Average discharge voltage during cycling of the electrode after 50 cycles annealed at different temperature. The inset shows the discharge capacity during cycling.

(C) The 1st and 50th charge-discharge curves of the samples after the initial cycle or 50 cycles and annealing at 300°C.

Hu et al.[37] observed large pores in the interior of the cycled particle due to oxygen release within particles, leading to the voltage fade. Croy et al.[21] proposed the formation of tetrahedral Li and the migration of TM for explaining the onset of voltage fading and hysteresis. Cell impedance growth due to surface side reactions and spinel-like phase formation can be well excluded in our study for the following reasons: (1) average charging voltage decreases at a similar rate as the discharging voltage, which suggests the voltage decay is not an impedance controlled process (Figure S15), and (2) after 50 cycles, a spinel-like phase on the surface of LR-NCM is only observed to be several nanometers thick (Figure S7C). In addition, TM migration to the Li layer is less than 4% during 50 cycles based on the ND refinement (Table S1), which is consistent with our TEM observations. Both results imply the migration of TM from the TM layer to the lithium layer is at least not the dominant factor for voltage degradation in our system. Instead, the data presented in this work demonstrate different types of defects are generated and accumulated in the structure of LR-NCM material during electrochemical cycling. And the cycled material is in a relatively higher-energy state. These phenomena are a general characteristic of this group of material and are independent of both synthesis method and TM stoichiometry. The influence of defect generation on the structural metastability and voltage decay can be explained in two aspects.

First, the energy of the system increases with the addition of the lithium vacancies in the TM layer, given that total lithium concentration in the structure keeps constant. To describe this phenomenon theoretically, first-principles calculations were applied to estimate the system energy using a supercell with composition $Li_{14}Ni_3Mn_7O_{24}$. In this model, there are two "excess" Li ions located in the TM layer. A specific $Li_{12/14}$ concentration with one oxygen vacancy was chosen to simulate the discharged state ($Li_{12}Ni_3Mn_7O_{23}$), in which around 1/7 of Li and 1/24 oxygen ions are absent in the structure. The full range of lithium configurations were tested with zero, one, or two Li vacancies in the TM layer. Li in the TM layer can more effectively shield electrostatic repulsion between anions due to smaller LiO_6 octahedral space than that in the Li layer. As a result, the Gibbs free energy per unit cell increases by ~1 eV when locating both vacancies in the TM layer compared with no Li vacancies in the TM layer (Figure S16). Therefore, the Gibbs free energy of the system rises with progression of the electrochemical process, as indicated by the black arrows in Figure 5A.

Second, the energy of the system increases with oxygen stacking sequence changes from ABCABC (O3 notation introduced by Delmas and co-workers[38]) to ABABAB (O1 notation). According to Radin et al.,[39] transformations between O3 and O1 are easily accomplished via gliding of the MO_2 layers. A stacking sequence perturbation mechanism has recently been proposed, originating through dislocation network formation.[12] The influence of the oxygen stacking sequence on the system energy in LR-NCM material was also investigated by first-principles calculations. For simplicity, a supercell model composed of three-formula units of $Li_{11}Ni_2Mn_5O_{18}$ was used for LR-NCM structure with different oxygen stacking sequence. The Gibbs free energy for O1 stacking is higher than that of O3 stacking for almost all tested delithiation compositions (Figure S17). Without any face sharing sites between Li and TM octahedra, O3 stacking structure is more stable. Note that the energy difference between O1 and O3 stacking is smaller at low lithium concentration since less face-sharing sites are filled. In fact, the preference for O1 upon complete delithiation has been confirmed to minimize overlap between the metal ion d orbitals and the oxygen p orbitals.[40] It is found not only in our work that O1 stackings once form at complete delithiation state do not fully

CellPress

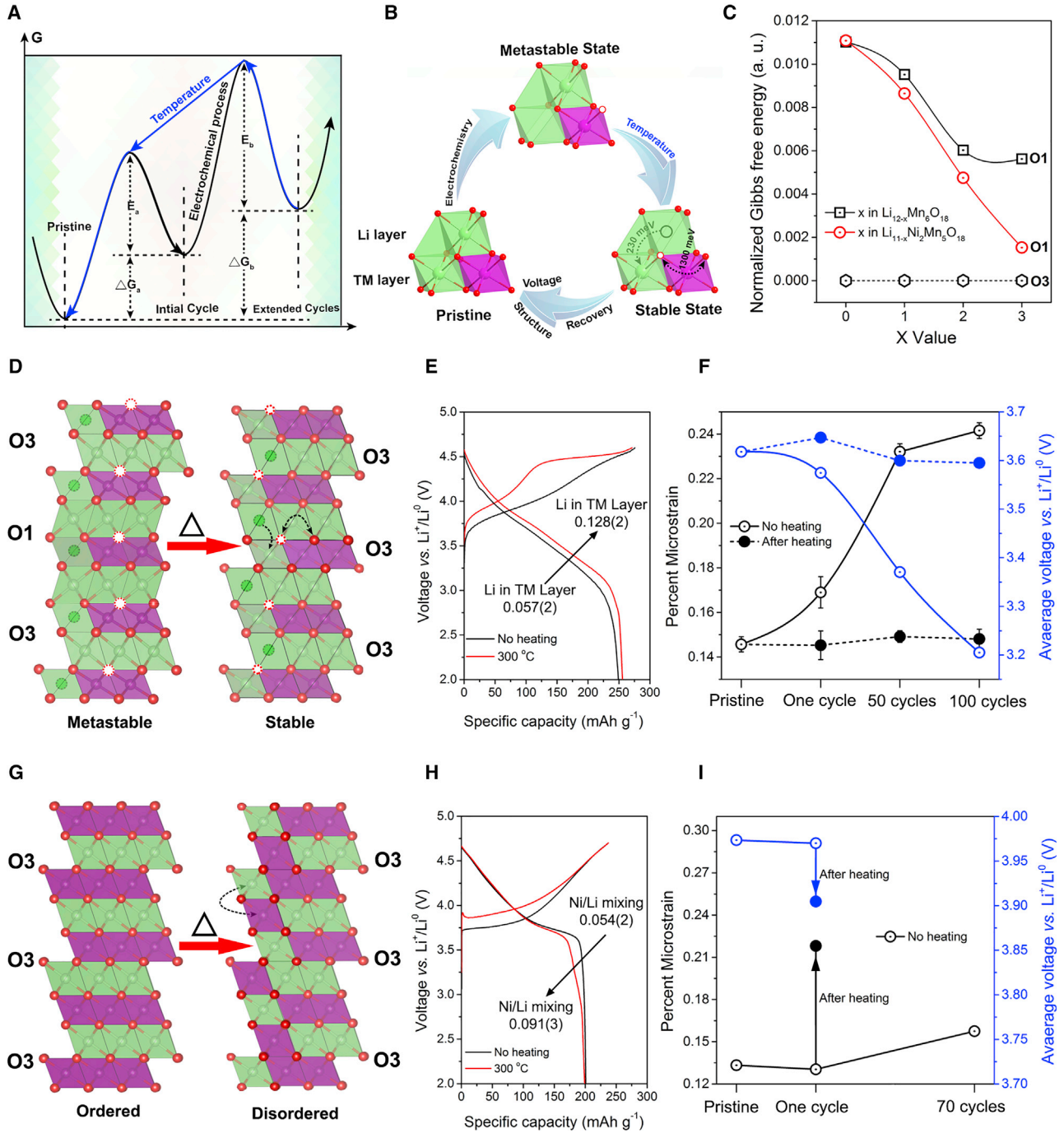

Figure 5. Mechanism Explanation for Cycled Structure Metastability and Reversibility of Anionic Redox-Based Cathode Materials

(A) Schematic illustration of the Gibbs free energy profiles for the conversion between pristine and cycled Li-rich layered oxides.

(B) Representation of adjacent Li and TM layer in Li-rich layered oxide structure as obtained from DFT calculations for different states. Li, Mn, and O atoms are represented in green, purple, and red, respectively. The MnO_6 polyhedron is shown to illustrate the oxygen vacancy migration induced by temperature, which facilitates Li ions reinsertion from lithium layer to the TM layer.

(C) Gibbs free energy difference due to stacking fault formation in Mn-based or NiMn-based Li-rich layered oxide material. Edge sharing between the Li and TM octahedral sites occurs in O3 stacking, while face sharing occurs in O1 stacking. In the phenomenological Gibbs free energy diagram, edge sharing octahedra result in the energetically favorable configuration and face sharing raises the energy, particularly for high lithium concentration.

(D and G) Schematic illustration of the structure evolution for cycled Li-rich layered oxide (D) and classic layered oxide (G) during heat treatment. Dashed circles represent vacant sites.

transform back to O3 stackings at lithiation state. Although there can be strong thermodynamic driving force for transformation from O1 to O3 stacking at lithiation state, the cycled material can be trapped in a metastable state with a large energy barrier to overcome. Both lithium vacancies in the TM layer and stacking sequence faults raise the system energy, creating metastable state of the cycled material. This energy difference is greater at high lithium concentration simply because there is more coulombic repulsion between Li-Li and Li-TM cations. Note that the slope of the Gibbs free energy as a function of lithium concentration is a rough estimate for the average voltage. This results in a smaller average voltage for the structure with more defects (Figure S17C). Therefore, voltage decay during cycling is clearly dominated by defect formation in the structure. Figure 5C further compares the Gibbs free energy difference due to stacking fault formation between Mn-based and NiMn-based Li-rich layered oxide material. In this plot, Gibbs free energy of O1 stacking is normalized to its O3 stacking analog for each of delithiation composition. The energy gap between O1 and O3 stacking thus represents how much the system is away from its stable state. Obviously, substitution of Mn by Ni could effectively prevent the deviation of the cycled state from the stable state, which indicates less voltage drop given the same amount of defects generation in the cycled structure. This result is consistent with our recent observations,[41] where the structure rigidity (reversibility) is achieved by cations with stronger covalency (e.g., Ni^{4+}) relative to those with stronger ionicity (e.g., Mn^{4+}).

The cycled state is a metastable state because of not only the relatively higher energy but also the large energy barrier (as labeled by E_a and E_b in Figure 5A); the system cannot easily overcome this barrier to relax toward the stable state through natural processes. On the one hand, in the calculated model $Li_{12}Ni_3Mn_7O_{23}$ for a metastable state (cycled state), oxygen vacancy sites are not directly coordinated to lithium vacancies in the TM layer in the structure with the lowest Gibbs free energy (Figure 5B). As confirmed by our previous calculations, Li-occupied tetrahedral sites, which are face-sharing with the Li vacancies in the TM layer, are most stable.[6] Such Li ions will be trapped in the tetrahedral site without diffusing into the adjacent octahedral site in the TM layer. However, if the oxygen vacancy can migrate to the shared plane between the tetrahedral site and the octahedral site, the under-coordinated Li tetrahedral site is no longer stable and will automatically relax back to the TM layer. To verify the possibility of this oxygen local migration, the nudged elastic band (NEB) method was used to find the vacancy migration barrier.[42] Five images between the initial and the final states were considered in the simulation. As shown in Figure S18, the local oxygen migration barrier is as high as 1,300 meV, which makes the oxygen vacancy migration process nearly impossible to occur at room temperature. Similar activation energy barriers (1,000–2,000 meV) for oxygen migration were predicted by Lee and Persson in Li-rich layered oxide Li_xMnO_3, depending on its Li content and hopping direction.[43] The hopping rates in migration paths were obtained by the Boltzmann relationship

$$\nu = \nu_0 \exp\left(\frac{-E_b}{k_B T}\right) \qquad \text{(Equation 1)}$$

(E and H) The first charge-discharge curves comparison of the initially cycled Li-rich layered oxide (E) and classic layered oxide (H) with or without annealing at 300°C. The classic layered oxide $LiNi_{1/3}Co_{1/3}Mn_{1/3}O_2$ were obtained from the initially cycled full batteries under the voltage range from 2.0 to 4.6 V and current density of 25 mA g^{-1} with graphite as anode material.

(F and I) Changes of percentage of microstrain and average voltage for LR-NCM and $LiNi_{1/3}Co_{1/3}Mn_{1/3}O_2$ after different cycles before and after heat treatment. The average voltage is obtained from the samples after different cycles annealed at 300°C for 1 h. Error bars represent standard errors.

where ν_0 is an attempt frequency. For the migration process in consideration, a 1,300 meV migration barrier at 300°C is equivalent to 650 meV at room temperature. As a comparison, high-temperature activation processes are universal in solid oxide fuel cells in which the oxygen conductor typically exhibits migration barriers around 1,000 meV.[44] Note that, unlike oxygen within fuel cells, which require long range bulk diffusion, local migration of oxygen at relatively lower temperature is feasible in the case of LR-NCM to eliminate Li vacancies in the TM layer. Under heat treatment, oxygen vacancy will be mobile in the cycled material and facilitate neighboring tetrahedral site Li hop to the TM layer to reach thermodynamically stable state. Then the same oxygen vacancy can migrate to another lattice position to exert the identical functionality. In principle, only small amounts of oxygen vacancies are required to alter the majority of tetrahedral site Li considering oxygen vacancies can continue to act repeatedly as structural catalyst. Concurrently, as demonstrated through TEM/ED, intermediate temperature (~300°C) annealing is an effective way to reduce stacking faults in the bulk structure. As a result, microstrain is reduced to almost the same minimum value after heat treatment no matter how long the samples have been cycled (Figure 5F). Through defect elimination, heat treatment serves as a driving force to enable the system to cross over the energy barrier, relaxing to the most stable state, as indicated by the blue arrows in Figure 5A. The energy reduction from the metastable state to stable state is released by an exothermic process as indicated in DTA measurement. Therefore, defect chemistry is the key control factor to achieve structure reversibility and voltage recovery.

It should be noted the metastable cycled state is the unique feature of LR-NCM particles, which enables thermal energy to play an effective role in structure and voltage recovery. However, for the cycled cathode material without anionic redox (Figure 5H; Figure S19), thermal energy can only introduce cation disordering. This follows the basic entropy principle that thermal energy increases the degree of system disorder. As a result, lower energy efficiency with larger overpotential is observed for the cycled classic layered oxide $LiNi_{1/3}Co_{1/3}Mn_{1/3}O_2$ annealed at 300°C. The direct comparison between cationic and anionic redox-based cathode material on the effect of thermal energy is illustrated in Figures 5D and 5G, which manifests uniqueness and complexity of anionic redox. Compared with Li-rich layered oxide, the cycled classic layered oxide contains fewer point defects in the TM layer and stacking faults along layers stacking direction. The lattice microstrain of $LiNi_{1/3}Co_{1/3}Mn_{1/3}O_2$ thus increases not as much as LR-NCM after extended cycles (Figure 5I). Cations migration during heat treatment for classic layered oxide occurs in terms of Li and TM position exchange since no vacant sites are created in the cycled state, assuming 100% Coulomb efficiency for simplicity (Figure 5G). The increase of disordering during heat treatment of cycled classic layered oxide is still dominant in the real case, in which small amount of vacant sites in the TM layer and stacking faults do exist. This explains the sharp increase of the lattice microstrain in Figure 5I for the initially cycled $LiNi_{1/3}Co_{1/3}Mn_{1/3}O_2$ during heat treatment. As for the Li-rich layered oxides, the transition from metastable state to stable state through mild heat treatment leads to system energy reduction in terms of entropy and disorder decrease (Figure 5D). One of the reasons for the direct contrast between cationic and anionic redox lies in the unique structural response to the anionic redox reaction. Our recent work has demonstrated the anisotropic O-O bonding evolution only occurs during the anionic redox region.[41] It is found that only the interlayer O-O distance is decreased while the intralayer O-O distance is well maintained during the anionic redox process, suggesting that the structural response to the anion redox is highly selective. This obvious local structure distortion

upon anionic redox can further induce a variety of defect formations, resulting in the unique metastable structure.

In summary, the structure metastability is responsible for the voltage decay in Li-rich layered oxides. Through combined SXRD, ND, (S)TEM, and first principles calculations on LR-NCM materials, this study pinpoints the critical influence of defect generation on the structural metastability and voltage decay. The metastability of the cycled structure is unique to cathode materials with anionic redox due to a variety of defects in different dimensions. More importantly, these findings suggest that defect elimination can help obviate the voltage decay issue. Based on the mechanistic description presented, we design a path, heat treatment, to remove the defects in the bulk structure. Such a treatment at intermediate temperature recovers the superstructure ordering and average discharge voltage. Although the heat treatment strategy is not that practical for direct industrial applications, this fundamental understanding of the structure metastability and reversibility will open up an opportunity to fully address the voltage decay issue of high-capacity Li-rich layered oxide cathodes.

EXPERIMENTAL PROCEDURES

Synthesis of Different Cathode Materials

The commercially available classic layered oxides $LiNi_{1/3}Co_{1/3}Mn_{1/3}O_2$ were purchased from Hunan Brunp Recycling Technology Co., Ltd. The detail synthesis procedure of Li-rich layered oxide $Li[Li_{0.144}Ni_{0.136}Co_{0.136}Mn_{0.544}]O_2$ was described in our previous report.[6] Stoichiometric amounts (4:1:1) of $NiSO_4 \cdot 6H_2O$, $CoSO_4 \cdot 7H_2O$, and $MnSO_4 \cdot 4H_2O$ were dissolved in the water to form a solution with the concentration of 2.0 mol L^{-1}. Then, a mixed solution of 2.0 mol L^{-1} Na_2CO_3 solution and 0.2 mol L^{-1} NH_4OH solution were pumped into a continuously stirred tank reactor (CSTR, capacity of 250 L) separately. The temperature of reactor was kept at 60°C, and the pH value of solution was controlled at 7.8. The resulting precipitates were $(Ni_{1/6}Co_{1/6}Mn_{4/6})CO_3$. To remove residual Na^+, precipitates were washed several times with distilled water. After being dried in a vacuum oven at 80°C for over 12 h, $(Ni_{1/6}Co_{1/6}Mn_{4/6})CO_3$ and Li_2CO_3 were thoroughly mixed with a molar ratio of 1:0.7 to form the precursor powders. The precursors were first heated at 500°C for 5 h, then calcinated at 850°C for 15 h in the air, and finally cooled to room temperature in the furnace. The detail synthesis procedure of cation-disordered rock-salt oxide $Li_{1.3}Nb_{0.3}Mn_{0.4}O_2$ was described in previous report.[9] The stoichiometric precursors containing Li_2CO_3, Nb_2O_5, and Mn_2O_3 were thoroughly mixed by wet mechanical ball milling and then dried in air. The as-obtained precursors were pressed into pellets with the pressure of 20 Mpa. The pellets were heated at 900°C for 12 h in an inert atmosphere.

Fabrication and Testing of Full Cells

The 5 Ah pouch cells with LR-NCM as cathode and Li metal as anode were first fabricated. The cathode contained 94.5 wt % LR-NCM, 3.0 wt % conductive carbon, and 2.5 wt % polyvinylidene fluoride (PVDF). The mass loading on each side of the cathode was about 25 mg cm^{-2}. The thickness of Li metal was 55 μm. The amount of electrolyte was 3 g/Ah. In addition, 18650-typed batteries (18 mm in diameter and 65 mm in height) were assembled in a similar way as reported previously.[45] The nominal capacity of the batteries was designed to 1,400 mAh. LR-NCM was used as cathode, $Li_4Ti_5O_{12}$@C (BTR, Shenzhen) as anode, and polyethylene as separator to fabricate the batteries. The cathode contained 94.5 wt % LR-NCM, 3.0 wt % conductive carbon, and 2.5 wt % PVDF. The mass loading on each side of the electrode was about 10 mg cm^{-2}. The anode contained 90.5 wt %

$Li_4Ti_5O_{12}$@C, 5.0 wt % conductive graphite, and 4.5 wt % PVDF. The mass loading on each side of the electrode was about 16 mg cm^{-2}. An electrolyte was then injected into the batteries in an argon filled glove box. LAND-CT2001B battery test systems were used to measure the initial charge-discharge and cycle performance of the batteries. For the initial cycle, the batteries in this study were directly charged and discharged between 3.25 to 0.5 V at 0.1 C. To measure the cycling performance, the constant-current constant-voltage (CC-CV) protocol was applied: all the batteries were cycled in the voltage range of 1.0–3.25 V versus $Li_4Ti_5O_{12}$ at 140 mA (0.1 C), where the batteries were charged with a constant current of 140 mA (0.1 C), followed by holding the voltage at 3.25 V until the current dropped to 70 mA (0.05 C). The fully discharged batteries at 1^{st} and 50^{th} cycle at 0.1 C-rate were dissembled in the glove box for further characterizations.

Electrochemical Measurements

The working electrodes were prepared by a mixture of the pristine or cycled samples, conductive carbon, and polyvinylidene fluoride (PVDF) binder with a weight ratio of 80:10:10 on an aluminum foil. As demonstrated in Figures S4B and S4C, both PVDF binder and conductive carbon do not decompose until 350°C under heat treatment. By adding binder and carbon to the cycled electrodes containing 94.5 wt % LR-NCM, 3.0 wt % conductive carbon, and 2.5 wt % PVDF, the new working electrodes were prepared with weight ratio of 80:10:10 on an aluminum foil. To remove the residual N-methyl-2-pyrrolidone (NMP) and traces of water, the electrode were dried at 80°C for 12 h in vacuum. Electrode discs of 13-mm diameter were punched from the working electrode. Lithium metal was used as the counter electrode, Celgard 2502 as the separator, and 1 mol L^{-1} $LiPF_6$ dissolved in ethylene carbonate (EC) dimethyl carbonate (DMC, Zhangjiagang Guotai-Huarong New Chemical Materials Co., Ltd.) with the volume ratio of 3:7 as electrolyte. The cells were assembled in an Ar-filled glove box (H_2O < 0.1 ppm, and O_2 < 0.1 ppm) and galvanostatically cycled on a LAND-CT2001A battery test system. All the tests were performed at room temperature.

Materials Characterizations

TG and DTA analysis (Pyris Diamond, Perkin-Elmer) from room temperature to 400°C at a rate of 2°C min^{-1} was conducted for the cycled samples under air or nitrogen stream, respectively. Morphology and chemical compositions were measured by Field emission scanning-electron microscope (Hitachi S-4800) with energy-dispersive X-ray spectroscopy (EDS). The detailed results are listed in Table S2, where we normalized the content of Ni as 1.000.

In Situ TD-SXRD

The cycled batteries were transferred to a glove box for disassembling. The cathodes were washed in DMC solvent in the glove box, and the mixed cathode powders (including the binder and conductive carbon) were obtained by scratching off the electrode from the current collector. The powders were loaded into 1.0 mm diameter corundum capillaries. The capillary was then mounted on the thermal stage of beamline 14B1, at Shanghai Synchrotron Radiation Facility (SSRF). The wavelength used at the 14B1 was 0.6887 Å (18 KeV). The detailed information about beamline BL14B1 can be found in their previous work.[46] To track the structural changes accompanied with the temperature changes, SXRD spectra continuously were recorded as a set of circles on a two-dimensional image plate detector in the transmission mode during heating from room temperature to 400°C (i.e., heating rate = 5°C min^{-1}). The total recording time for one spectrum was approximately 30 s. The microstrain was analyzed by examining line broadening observed in the

SXRD patterns. Williamson-Hall analysis of all peaks that exhibit the best linear fitting was carried out for a quantification of microstrain changes during the heat treatment by the following equation:

$$FW(S) \times \cos(\theta) = \frac{K \times \lambda}{Size} + 4 \times Strain \times \sin(\theta) \quad \text{(Equation 2)}$$

where $FW(S)$ is the calculated full-widths for the sample, K is the crystallite shape factor and was set to be 0.9, the diffraction angle is given by θ, and λ is the X-ray wavelength of the source. The strain is then extracted from the slope of the plot of $FW(S)\cos(\theta)$ versus $4\sin(\theta)$.

Ex Situ ND

The cycled powder samples annealed at different temperature were carried out by the *ex situ* ND. The data of samples after the initial cycle were collected on the VULCAN beamline at the Spallation Neutron Sources (SNS) in the Oak Ridge National Laboratory (ORNL).[47] The sample was packed into a vanadium can. An incident beam (5 mm × 12 mm) was employed with 0.7 to 3.5 Å bandwidth, which allowed a 0.5∼2.5 Å d-spacing in the diffracted patterns in the $\pm 90^{\circ}$ 2θ detector banks. The double-disk choppers at a speed of 30 Hz were selected. A high-resolution mode was applied with $\Delta d/d \sim 0.25\%$. The SNS was at a nominal 1,100 kW. Powder-neutron-diffraction data were collected at a high-resolution mode for 3 h and reduced by the VDRIVE software. Samples after 50 cycles were loaded into separate vanadium sample cells inside a helium-purged glove box and sealed with an indium O-ring. The constant wavelength ND measurements were conducted on the lithium containing samples using a Ge(733) monochromator with an in-pile 60′ collimator, corresponding to a neutron wavelength of 1.19690 Å, using the high-resolution neutron powder diffractometer, BT-1 at the National Institute of Standards and Technology Center for Neutron Research (NCNR). Diffraction measurements were all conducted at room temperature (T = 295 K). The GSAS program with the EXPGUI interface was used to perform full-pattern Rietveld refinement.[48]

Ex Situ (S)TEM/ED

For *ex situ* TEM heating experiment, the LR-NCM particles, collected from the electrode past the first cycle, were dispersed in an organic solvent and dropped onto a carbon-support-film-coated copper mesh TEM grid. After the initial TEM investigation, the experimented grid was heated at 300°C for 1 h in an air oven with heating rate of 10°C /min. After the heating, the grid was cooled down slowly in the oven. The same particles observed during the initial TEM experiment were investigated again by TEM for the comparison. Even though it is not an easy task, we have the skill to track the same particle with *ex situ* TEM measurement.[49] The ED patterns and high-resolution STEM images were obtained from a double aberration-corrected JEOL-ARM 200CF microscope (at Brookhaven National Laboratory) with a cold-field emission gun operated at 200 keV. For ED simulation using the SingleCrystal program, we assumed stacking faults were allowed only in between the −O−TM−O−Li− slabs and could never be generated inside the slabs. Three vectors defined as [0, 0, 1], [1/2, −1/6, 1], and [1/6, −1/6, 1] in the unit cell $Li_{14}Ni_3Mn_7O_{24}$ (the same structure model applied in first principles calculations) with conventional monoclinic cell definition represent all possible atomic configurations generated by the stacking faults.[50] Different concentration of stacking faults was associated with the stacking probabilities of these stacking vectors.

Ex Situ XAS

The initially cycled LR-NCM electrodes annealing at different temperatures (room temperature, 100°C, 150°C, 200°C, 250°C, and 300°C) for 1 h were used for XAS measurements. The Ni, Co, and Mn K-edges were carried out in transmission mode at the KMC-2 beamline of the synchrotron BESSY at Helmholtz-Zentrum Berlin, Germany, using a graded Si-Ge (111) double-crystal monochromator. In order to eliminate the high-order harmonics, about 65% of the maximum possible intensity of the beam is transmitted through the sample during the measurements. Ni, Co, and Mn foils were measured simultaneously with each sample for energy calibration. The data were analyzed though using the software ATHENA of the package IFEFFIT as reported in the literature. Each spectrum was energy-calibrated with respect to the first inflection point in their corresponding reference metal foil spectrum. The normalized EXAFS signal was Fourier transformed in R space without phase shift correction.

Computation Methodology

First-principles calculations were performed in the spin polarized GGA+U approximations to the Density Functional Theory (DFT) as implemented in the Vienna *ab initio* simulation package.[51,52] The same effective U value as applied in our previous report was used to enforce the effect of localized d electrons of the transition-metal ions.[53] We used the Perdew-Burke-Ernzerhof exchange correlation and a plane-wave representation for the wave function with a cutoff energy of 450 eV.[54] The Brillouin zone was sampled with a dense k-points mesh by Gamma packing. To obtain the Gibbs free energy for different lithium vacancy configurations, the atomic positions and cell parameters were fully relaxed. Assuming that the entropic and volumetric effects are small at low temperature, the Gibbs free energy change for different structure model is approximated by the DFT calculated total energy. In our previous work, different models of fully lithiated $Li_{14}Ni_3Mn_7O_{24}$ were created, and the calculated total energies are compared.[20] In the model with the lowest energy, the Li layer is composed of 12 Li ions, and the in-plane cation ordering of the TM layer is shown in Figure S20A. The same fully lithiated structure model was employed in this work. As shown in Figure S21, the presence of the Li-O-Li linear configuration in the fully lithiated structure $Li_{14}Ni_3Mn_7O_{24}$ shows a greatly increased 2p density of states within 1.5 eV of the Fermi energy, which is the signature for oxygen redox during the delithiation process. Then, the full range of different configurations were tested with zero, one, or two Li vacancies in the TM layer for the delithiated structure $Li_{12}Ni_3Mn_7O_{24}$. Figure S20 shows the structure model for each case with the lowest energy. And then one oxygen vacancy was created in each of the case to simulate the discharged state ($Li_{12}Ni_3Mn_7O_{23}$). The oxygen vacant site was fixed based on our previous study, where the most labile oxygen was observed computationally through the increased density of states below the Fermi level of oxygen atoms.[55] The voltage for stacking sequence O3 and O1 was calculated from Nernst equation:

$$Voltage\ \left(vs\ Li\,/\,Li^{+}\right) = \frac{\mu_{Li}^{anode} - \mu_{Li}^{cathode}}{ne} \qquad \text{(Equation 3)}$$

where $\mu_{Li}^{cathode}$ is the chemical potential per atom of Li in the cathode, μ_{Li}^{anode} is the chemical potential per atom of Li in the anode and equals to −1.9 eV, and ne is the number of transferred electrons per lithium atom. The chemical potential of Li ions in cathode ground state structures at each Li concentration can be approximated by:

$$\mu_{Li}^{Li_{11-x}Ni_2Mn_5O_{18}} = \frac{dG_{Li_{11-x}Ni_2Mn_5O_{18}}}{dN_{Li}} \approx G_{Li_{(11-x)+1}Ni_2Mn_5O_{18}} - G_{Li_{11-x}Ni_2Mn_5O_{18}} \qquad \text{(Equation 4)}$$

The ground state structures are the vertices of the formation enthalpies convex hull that defines the minimal energy as a function of composition. Note that the unit cell structure model $Li_{11-x}Ni_2Mn_5O_{18}$ ($x \leq 4$) was applied to determine the most energy favorable lithium vacancies configurations for each delithiation step. The lithium vacancies configurations were thoroughly tested, and the structure model for the lowest energy state is shown in Figure S22. And then a supercell model composed of three-formula units of $Li_{11-x}Ni_2Mn_5O_{18}$ was built with different oxygen stacking sequence. The NEB method was used to find the minimum-energy path and the energy barrier for oxygen migration inside the materials.

DATA AND CODE AVAILABILITY

The authors declare that data supporting the findings of this study are available within the paper and the Supplemental Information. All other data are available from the lead contact upon reasonable request.

SUPPLEMENTAL INFORMATION

Supplemental Information can be found online at https://doi.org/10.1016/j.xcrp.2020.100028.

ACKNOWLEDGMENTS

NIMTE's work is supported by the National Key Research and Development Program of China (Grant No. 2016YFB0100100), the National Natural Science Foundation of China (Grant No. 21703271 and 21773279), and Key projects in Cooperation between CAS and Department of Energy, USA (CAS-DOE, Grant No. 174433KYSB20150047). UC San Diego's efforts are supported by the Assistant Secretary for Energy Efficiency and Renewable Energy, Office of Vehicle Technologies of the U.S. Department of Energy (DOE) under Contract No. DE-AC02-05CH11231, Subcontract No. 7073923, under the Advanced Battery Materials Research (BMR) Program. Work at BNL is supported by US DOE, Basic Energy Sciences, Materials Sciences and Engineering Division under Contract No. DE-SC0012704. B.Q. acknowledges the support from National Postdoctoral Program for Innovative Talents (Grant No. BX201600176) and China Postdoctoral Science Foundation (Grant No. 2017M612044). The authors thank beamline BL14B1 (Shanghai Synchrotron Radiation Facility) for providing the beam time and assistance. The neutron experiments benefit from the SNS user facilities (VULCAN beamline) sponsored by the office of Basic Energy Sciences (BES), the Office of Science of the US DOE. The computation work using the Extreme Science and Engineering Discovery Environment (XSEDE) is supported by National Science Foundation grant number ACI-1548562. The authors thank Dr. Yonggao Xia from NIMTE for the experimental discussion and Dr. An and Dr. Chen from SNS for the technique support of neutron experiment.

AUTHOR CONTRIBUTIONS

B.Q. designed the experiments. M.Z., B.Q., and Y.S.M. performed the mechanism analysis. S.-Y.L., L.W., and Y.Z. performed the electron microscopy imaging, diffraction, and analysis. B.Q. and W.W. conducted the synchrotron X-ray diffraction measurements. M.Z. and T.A.W. performed the first-principles calculations. D.Z. performed the *ex situ* X-ray adsorption spectroscopy measurements. H.L. and C.M.B. performed ND experiment and data analysis. Z.L. and Y.S.M. supervised the research. B.Q. and M.Z. co-wrote the manuscript. All authors contributed to the discussion and provided feedback on the manuscript.

DECLARATION OF INTERESTS

The authors declare no competing interests.

Received: October 7, 2019
Revised: December 13, 2019
Accepted: January 16, 2020
Published: March 11, 2020

REFERENCES

1. Armand, M., and Tarascon, J.-M. (2008). Building better batteries. Nature *451*, 652–657.
2. Palacín, M.R. (2009). Recent advances in rechargeable battery materials: a chemist's perspective. Chem. Soc. Rev. *38*, 2565–2575.
3. Whittingham, M.S. (2014). Ultimate limits to intercalation reactions for lithium batteries. Chem. Rev. *114*, 11414–11443.
4. Saubanère, M., McCalla, E., Tarascon, J.M., and Doublet, M.L. (2016). The intriguing question of anionic redox in high-energy density cathodes for Li-ion batteries. Energy Environ. Sci. *9*, 984–991.
5. Seo, D.H., Lee, J., Urban, A., Malik, R., Kang, S., and Ceder, G. (2016). The structural and chemical origin of the oxygen redox activity in layered and cation-disordered Li-excess cathode materials. Nat. Chem. *8*, 692–697.
6. Qiu, B., Zhang, M., Xia, Y., Liu, Z., and Meng, Y.S. (2017). Understanding and controlling anionic electrochemical activity in high-capacity oxides for next generation Li-ion batteries. Chem. Mater. *29*, 908–915.
7. Luo, K., Roberts, M.R., Hao, R., Guerrini, N., Pickup, D.M., Liu, Y.S., Edström, K., Guo, J., Chadwick, A.V., Duda, L.C., and Bruce, P.G. (2016). Charge-compensation in 3d-transition-metal-oxide intercalation cathodes through the generation of localized electron holes on oxygen. Nat. Chem. *8*, 684–691.
8. Qiu, B., Zhang, M., Wu, L., Wang, J., Xia, Y., Qian, D., Liu, H., Hy, S., Chen, Y., An, K., et al. (2016). Gas-solid interfacial modification of oxygen activity in layered oxide cathodes for lithium-ion batteries. Nat. Commun. *7*, 12108.
9. Yabuuchi, N., Nakayama, M., Takeuchi, M., Komaba, S., Hashimoto, Y., Mukai, T., Shiiba, H., Sato, K., Kobayashi, Y., Nakao, A., et al. (2016). Origin of stabilization and destabilization in solid-state redox reaction of oxide ions for lithium-ion batteries. Nat. Commun. *7*, 13814.
10. Bre'ger, J., Meng, Y.S., Hinuma, Y., Kumar, S., Kang, K., Shao-Horn, Y., Ceder, G., and Grey, C.P. (2006). Effect of high voltage on the structure and electrochemistry of $LiNi_{0.5}Mn_{0.5}O_2$: A joint experimental and theoretical study. Chem. Mater. *18*, 4768–4781.
11. Jiang, M., Key, B., Meng, Y.S., and Grey, C.P. (2009). Electrochemical and structural study of the layered, "Li-excess" lithium-ion battery electrode material $Li[L_{11/9}Ni_{1/3}Mn_{5/9}]O_2$. Chem. Mater. *21*, 2733–2745.
12. Singer, A., Hy, S., Zhang, M., Cela, D., Fang, C., Qiu, B., Xia, Y., Liu, Z., Ulvestad, A., Hua, N., et al. (2018). Nucleation of dislocations and their dynamics in layered oxides cathode materials during battery charging. Nat. Energy *3*, 641–647.
13. Jarvis, K.A., Deng, Z., Allard, L.F., Manthiram, A., and Ferreira, P.J. (2011). Atomic structure of a lithium-rich layered oxide material for lithium-ion batteries: evidence of a solid solution. Chem. Mater. *23*, 3614–3621.
14. Fell, C.R., Chi, M., Meng, Y.S., and Jones, J.L. (2012). In situ X-ray diffraction study of the lithium excess layered oxide compound Li $[Li_{0.2}Ni_{0.2}Mn_{0.6}]O_2$ during electrochemical cycling. Solid State Ion. *207*, 44–49.
15. Croy, J.R., Gallagher, K.G., Balasubramanian, M., Chen, Z., Ren, Y., Kim, D., Kang, S.-H., Dees, D.W., and Thackeray, M.M. (2013). Examining hysteresis in composite $xLi_2MnO_3 \cdot (1-x)LiMO_2$ cathode structures. J. Phys. Chem. C *117*, 6525–6536.
16. Mohanty, D., Sefat, A.S., Li, J., Meisner, R.A., Rondinone, A.J., Payzant, E.A., Abraham, D.P., Wood, D.L., 3rd, and Daniel, C. (2013). Correlating cation ordering and voltage fade in a lithium-manganese-rich lithium-ion battery cathode oxide: a joint magnetic susceptibility and TEM study. Phys. Chem. Chem. Phys. *15*, 19496–19509.
17. Qian, D., Xu, B., Chi, M., and Meng, Y.S. (2014). Uncovering the roles of oxygen vacancies in cation migration in lithium excess layered oxides. Phys. Chem. Chem. Phys. *16*, 14665–14668.
18. Genevois, C., Koga, H., Croguennec, L., Ménétrier, M., Delmas, C., and Weill, F. (2015). Insight into the atomic structure of cycled lithium-rich layered oxide $Li_{1.20}Mn_{0.54}Co_{0.13}Ni_{0.13}O_2$ using HAADF STEM and electron nanodiffraction. J. Phys. Chem. C *119*, 75–83.
19. Mohanty, D., Li, J., Abraham, D.P., Huq, A., Payzant, E.A., Wood, D.L., and Daniel, C. (2014). Unraveling the voltage-fade mechanism in high-energy-density lithium-ion batteries: origin of the tetrahedral cations for spinel conversion. Chem. Mater. *26*, 6272–6280.
20. Xu, B., Fell, C.R., Chi, M., and Meng, Y.S. (2011). Identifying surface structural changes in layered Li-excess nickel manganese oxides in high voltage lithium ion batteries: A joint experimental and theoretical study. Energy Environ. Sci. *4*, 2223–2233.
21. Croy, J.R., Balasubramanian, M., Gallagher, K.G., and Burrell, A.K. (2015). Review of the U.S. Department of Energy's "deep dive" effort to understand voltage fade in Li- and Mn-rich cathodes. Acc. Chem. Res. *48*, 2813–2821.
22. Oh, P., Ko, M., Myeong, S., Kim, Y., and Cho, J. (2014). A novel surface treatment method and new insight into discharge voltage deterioration for high-performance $0.4Li_2MnO_3$-$0.6LiNi_{1/3}Co_{1/3}Mn_{1/3}O_2$ cathode materials. Adv. Energy Mater. *4*, 201400631.
23. Zheng, F., Yang, C., Xiong, X., Xiong, J., Hu, R., Chen, Y., and Liu, M. (2015). Nanoscale surface modification of lithium-rich layered-oxide composite cathodes for suppressing voltage fade. Angew. Chem. Int. Ed. Engl. *54*,, 13058–13062.
24. Sathiya, M., Abakumov, A.M., Foix, D., Rousse, G., Ramesha, K., Saubanère, M., Doublet, M.L., Vezin, H., Laisa, C.P., Prakash, A.S., et al. (2015). Origin of voltage decay in high-capacity layered oxide electrodes. Nat. Mater. *14*, 230–238.
25. Yu, Z., Shang, S.-L., Gordin, M.L., Mousharraf, A., Liu, Z.-K., and Wang, D. (2015). Ti-substituted $Li[Li_{0.26}Mn_{0.6-x}Ti_xNi_{0.07}Co_{0.07}]O_2$ layered cathode material with improved structural stability and suppressed voltage fading. J. Mater. Chem. A Mater. Energy Sustain. *3*, 17376–17384.
26. Hy, S., Liu, H., Zhang, M., Qian, D., Hwang, B.-J., and Meng, Y.S. (2016). Performance and design considerations for lithium excess layered oxide positive electrode materials for lithium ion batteries. Energy Environ. Sci. *9*, 1931–1954.
27. Liu, H., Chen, Y., Hy, S., An, K., Venkatachalam, S., Qian, D., Zhang, M., and Meng, Y.S. (2016). Operando lithium dynamics in the Li-rich layered oxide cathode material via neutron diffraction. Adv. Energy Mater. Published online January 25, 2016. https://doi.org/10.1002/aenm.201502143.
28. Dogan, F., Long, B.R., Croy, J.R., Gallagher, K.G., Iddir, H., Russell, J.T., Balasubramanian, M., and Key, B. (2015). Re-entrant lithium local environments and defect driven electrochemistry of Li- and Mn-rich Li-ion battery cathodes. J. Am. Chem. Soc. *137*, 2328–2335.
29. Malashenko, V.V. (2015). Dynamic instability of dislocation motion at high-strain-rate deformation of crystals with high concentration of point defects. Phys. Solid State *57*, 2461–2463.
30. Yabuuchi, N., Kim, Y.-T., Li, H.H., and Shao-Horn, Y. (2008). Thermal instability of cycled $Li_xNi_{0.5}Mn_{0.5}O_2$ electrodes: an in situ synchrotron X-ray powder diffraction study. Chem. Mater. *20*, 4936–4951.
31. Geder, J., Song, J.H., Kang, S.H., and Yu, D.Y.W. (2014). Thermal stability of lithium-rich

manganese-based cathode. Solid State Ion. *268*, 242–246.

32. Williamson, G.K., and Hall, W.H. (1953). X-ray line broadening from filed aluminium and wolfram. Acta Metall. *1*, 22–31.

33. Bareño, J., Lei, C.H., Wen, J.G., Kang, S.H., Petrov, I., and Abraham, D.P. (2010). Local structure of layered oxide electrode materials for lithium-ion batteries. Adv. Mater. *22*, 1122–1127.

34. Hy, S., Felix, F., Rick, J., Su, W.N., and Hwang, B.J. (2014). Direct in situ observation of Li_2O evolution on Li-rich high-capacity cathode material, $Li[Ni_{(x)}Li_{((1-2x)/3)}Mn_{((2-x)/3)}]O_2$ ($0 \leq x \leq 0.5$). J. Am. Chem. Soc. *136*, 999–1007.

35. Yan, P., Nie, A., Zheng, J., Zhou, Y., Lu, D., Zhang, X., Xu, R., Belharouak, I., Zu, X., Xiao, J., et al. (2015). Evolution of lattice structure and chemical composition of the surface reconstruction layer in $Li_{(1.2)}Ni_{(0.2)}Mn_{(0.6)}O_2$ cathode material for lithium ion batteries. Nano Lett. *15*, 514–522.

36. Boulineau, A., Simonin, L., Colin, J.F., Bourbon, C., and Patoux, S. (2013). First evidence of manganese-nickel segregation and densification upon cycling in Li-rich layered oxides for lithium batteries. Nano Lett. *13*, 3857–3863.

37. Hu, E., Yu, X., Lin, R., Bi, X., Lu, J., Bak, S., Nam, K.-W., Xin, H.L., Jaye, C., Fischer, D.A., et al. (2018). Evolution of redox couples in Li- and Mn-rich cathode materials and mitigation of voltage fade by reducing oxygen release. Nat. Energy *3*, 690–698.

38. Delmas, C., Fouassier, C., and Hagenmuller, P. (1980). Structural classification and properties of the layered oxides. Physica B+C *99*, 81–85.

39. Radin, M.D., Hy, S., Sina, M., Fang, C., Liu, H., Vinckeviciute, J., Zhang, M., Whittingham, M.S., Meng, Y.S., and Van der Ven, A. (2017). Narrowing the gap between theoretical and practical capacities in Li-ion layered oxide cathode materials. Adv. Energy Mater. *7*, 1602888.

40. Croguennec, L., Pouillerie, C., Mansour, A.N., and Delmas, C. (2001). Structural characterisation of the highly deintercalated $Li_xNi_{1.02}O_2$ phases (with $x \leq 0.30$). J. Mater. Chem. *11*, 131–141.

41. Zhao, E.Y., Zhang, M., Wang, X.L., Hu, E.Y., Liu, J., Yu, X.Q., Olguin, M., Wynn, T.A., Meng, Y.S., Page, K., et al. (2019). Local structure adaptability through multi cations for oxygen redox accommodation in Li-Rich layered oxides. Energy Storage Materials *24*, 384–393.

42. Mills, G., and Jónsson, H. (1994). Quantum and thermal effects in H2 dissociative adsorption: Evaluation of free energy barriers in multidimensional quantum systems. Phys. Rev. Lett. *72*, 1124–1127.

43. Lee, E., and Persson, K.A. (2014). Structural and chemical evolution of the layered Li-excess Li_xMnO_3 as a function of Li content from First-principles calculations. Adv. Energy Mater. *4*, 1400498.

44. Kushima, A., and Yildiz, B. (2010). Oxygen ion diffusivity in strained yttria stabilized zirconia: where is the fastest strain? J. Mater. Chem. *20*, 4809.

45. Qiu, B., Zhang, Q., Hu, H., Wang, J., Liu, J., Xia, Y., Zeng, Y., Wang, X., and Liu, Z. (2014). Electrochemical investigation of Li-excess layered oxide cathode materials/mesocarbon microbead in 18650 batteries. Electrochim. Acta *123*, 317–324.

46. Yang, T., Wen, W., and Yin, G. (2015). Introduction of the X-ray diffraction beamline of SSRF. Nucl. Sci. Tech. *26*, 020101.

47. An, K., Wang, X.L., and Stoica, A.D. (2012). Vulcan data reduction and interactive visualization software (ORNL Report ORNL-TM-2012-621).

48. Toby, B.H. (2001). EXPGUI, a graphical user interface for GSAS. J. Appl. Cryst. *34*, 210–213.

49. Lee, S.-Y., Park, K.-Y., Kim, W.-S., Yoon, S., Hong, S.-H., Kang, K., and Kim, M. (2016). Unveiling origin of additional capacity of SnO_2 anode in lithium-ion batteries by realistic ex situ TEM analysis. Nano Energy *19*, 234–245.

50. Boulineau, A., Croguennec, L., Delmas, C., and Weill, F. (2010). Structure of Li_2MnO_3 with different degrees of defects. Solid State Ion. *180*, 1652–1659.

51. Kresse, G., and Furthmiiller, J. (1996). Efficiency of ab-initio total energy calculations for metals and semiconductors using a plane-wave basis set. Comput. Mater. Sci. *6*, 15–50.

52. Kresse, G., and Joubert, D. (1999). From ultrasoft pseudopotentials to the projector augmented-wave method. Phys. Rev. B Condens. Matter Mater. Phys. *59*, 1758–1775.

53. Hinuma, Y., Meng, Y.S., Kang, K., and Ceder, G. (2007). Phase transitions in the $LiNi_{0.5}Mn_{0.5}O_2$ system with temperature. Chem. Mater. *19*, 1790–1800.

54. Perdew, J.P., Burke, K., and Ernzerhof, M. (1996). Generalized gradient approximation made simple. Phys. Rev. Lett. *77*, 3865–3868.

55. Wynn, T.A., Fang, C., Zhang, M., Liu, H., Davies, D.M., Wang, X., Lau, D., Lee, J.Z., Huang, B.-Y., Fung, K.Z., et al. (2018). Mitigating oxygen release in anionic-redox-active cathode materials by cationic substitution through rational design. J. Mater. Chem. A Mater. Energy Sustain. *6*, 24651–24659.